New insight into the microstructure of natural calcined laterites and their performance as heterogeneous Fenton catalyst for methylene blue degradation

Gloria Murielle Rostandi Kpinsoton, Héla Karoui, Yohan Richardson, Blédja N'dri Stéphanie Koffi, Hamma Yacouba, Julius Motuzas, Martin Drobek, Abdou Lawane Gana

New insight into the microstructure of natural calcined laterites and their performance as heterogeneous Fenton catalyst for methylene blue degradation

Gloria Murielle Rostandi KPINSOTON[1,2], Héla KAROUI[1], Yohan RICHARDSON[2*], Blédja N'dri Stéphanie KOFFI[1], Hamma YACOUBA[3], Julius MOTUZAS[4], Martin DROBEK[5], Abdou LAWANE GANA[6]

1. Institut International d'Ingénierie de l'Eau et de l'Environnement (2iE), Laboratoire Eau Dépollution Ecosystème et Santé (LEDES), Rue de la Science, 01 BP 594 Ouagadougou 01, Burkina Faso.
2. Institut International d'Ingénierie de l'Eau et de l'Environnement (2iE), Laboratoire Biomasse Energie et Biocarburants (LBEB), Rue de la Science, 01 BP 594 Ouagadougou 01, Burkina Faso.
3. Institut International d'Ingénierie de l'Eau et de l'Environnement (2iE), Laboratoire Hydrologie et Ressources en Eau (LEAH), Rue de la Science, 01 BP 594 Ouagadougou 01, Burkina Faso.
4. The University of Queensland, FIM2Lab – Functional Interfacial Materials and Membranes, School of Chemical Engineering, Brisbane, Qld 4072, Australia.
5. Institut Européen des Membranes, UMR 5635, Université de Montpellier, ENSCM, CNRS, Place Eugène Bataillon, F-34095 Montpellier cedex 5, France.
6. Institut International d'Ingénierie de l'Eau et de l'Environnement (2iE), Laboratoire Eco-matériaux de construction (LEMC), Rue de la Science, 01 BP 594 Ouagadougou 01, Burkina Faso.

*corresponding author: Yohan RICHARDSON. Email : richardson.yohan@gmail.com

Abstract

In this work, natural laterites from Burkina Faso were calcined at different temperatures in the range 400-800°C. XRD, EDS, N_2 adsorption manometry and TGA-DSC analyses together with a thorough analysis of available literature data, support that the laterite sample consists mainly of goethite and hematite embedded in a framework of kaolinite and quartz with different interaction extents. During calcination up to 400°C, the kaolinite structure is partially destroyed due to loss of structural water and the goethite phase previously in association with the kaolinite lattice transforms into free hematite crystallites, resulting in a drop of the surface area of the composite material. At 600°C, the kaolinite lattice is further deshydroxylated leading to an amorphous metakaolin matrix containing mainly surface hematite nanophases. Despite a substantial reduction of the surface area due to the calcination-induced shrinkage of alumino-silicate framework, the laterite calcined at 600°C exhibits the highest performance in the methylene blue (MB) degradation by the Fenton process with a degradation rate of 99 % after 100 minutes of treatment at room temperature. The effects of solution pH, H_2O_2 concentration, initial MB concentration and catalyst dosage were investigated. A slight but significant visible light induced removal enhancement effect suggested a visible photocatalytic activity of the hematite phase. The calcined laterite demonstrates a strong catalytic stability over several utilizations therefore is worth to be seriously considered in the design of sustainable and readily affordable wastewater treatment solutions in developing tropical countries.

Keywords: Laterite, iron oxides, heterogeneous Fenton catalysts, methylene blue degradation

Introduction

Textile industries generate large volumes of wastewater which acts as pollution source. There are over 100,000 types of commercially available dyes with a production rate higher than 800,000 ton per year [1]. Approximately 10 - 50 per cent of dyes loss is observed during dyeing. Several dyes used in the textile industries are reluctant to conventional biodegradation processes [2]. Several methods are used for treatment of dye contained in wastewater. Some physical-chemical methods like electrocoagulation [3] and adsorption [4] have been used successfully for methylene blue removal. These methods are non-destructive thus inappropriate for the dye degradation. Fenton processes have been widely studied as advanced oxidation processes based on one of the most powerful oxidant, the hydroxyl radicals in aqueous solution. In the pristine and classical Fenton process technology, these radicals are generated by the well-known Fenton reaction involving hydrogen peroxide (H_2O_2) and aqueous ferrous ions. The classical Fenton process has proved to be an effective technology for the degradation of many organic pollutants that are bioreluctant. However, several disadvantages arise in its practical application. The main disadvantages of the classical Fenton process are (i) the restricted operational pH range centered around 3 and (ii) the generation of a high amount of iron sludge [5, 6]. In order to overcome these drawbacks, research efforts have been oriented towards the development of heterogeneous Fenton processes. In this case, a solid containing active iron species is used instead of ferrous ions in the classical homogeneous Fenton process. Various types of solids have been considered as heterogeneous Fenton catalysts for the degradation of organic pollutants and have been recently reviewed [7, 8]. From a practical point of view, they can be divided in two lumps of catalysts: synthetic catalysts and natural catalysts. The use of natural catalysts are gaining increasing attention considering both economic and environmental standpoints [9] and benefits from the progress of the scientific understanding of the complex catalytic mechanisms underlying the heterogeneous Fenton process thanks to theoretical studies on well-defined synthetic solid catalysts [10]. Due to their low cost, abundance and ecofriendly nature, clays and iron minerals have been proposed as a promising alternative to synthetic catalysts for the decontamination of soils, groundwaters, sediments and wastewater effluents [9, 11–14]. Clays that naturally contain iron species has been successfully used for the heterogeneous Fenton-like oxidation of phenol [15]. Recently, laterite, another natural soil material containing naturally significant amount of iron oxides has attracted attention of some researchers as a source of iron for both homogeneous and heterogeneous Fenton processes [16–21]. Laterite is an important natural source of iron widely available in several parts of the world especially in tropical zones and covers about one third of the lands [22, 23]. Moreover, laterite has considerably low cost, is nontoxic for the environment and exhibits a relatively high thermal and chemical stability [24]. These advantages make it an economically appealing and sustainable alternative to both the classical Fenton process and the expensive synthetic heterogeneous Fenton catalysts. In spite of these advantages, laterite has attracted little attention and a very few work on the use of laterite as a source of iron for Fenton processes within the last ten years. The first research work was focused on the use of laterite as an iron source for the homogeneous Fenton process [16, 17]. This approach is of certain interest insofar industrial iron can be substituted by iron readily extracted from an abundant and local source of iron, however do not eliminate the drawbacks associated with the classical Fenton process. More recently, Khataee et al. demonstrated the potential of an iron-rich laterite soil, raw or calcined at 350 °C as a heterogeneous Fenton catalyst for the degradation of sodium azide or an azo dye [18, 19]. Although the catalytic activity has been attributed to the occurrence of iron oxides phases in the laterite-based materials, there is a lack of knowledge on the microstructure-catalytic activity relationships due to the complexity of this kind of natural iron oxides supported catalysts while being fundamental to improve the process efficiency. In particular, the role of calcination in the microstructure of the resulting materials is not very clear.

Recently, Kenda et al. [25], reported in their work the phase changes in laterites calcined at temperatures ranging from 400°C to 1200°C. Interestingly, it was evidenced the formation of magnetite through melting up at up to 1000°C and subsequent recrystallization. The magnetite phase is of particular interest in the heterogeneous Fenton process considering its higher ability for degradation of recalcitrant pollutants compared to iron III oxide phases due to the presence of both Fe(II) et Fe(III) species [26]. However, such a treatment is high energy consuming and limits its practical application. Therefore, it is worth to first assess the potential of using laterite calcined at lower temperatures, insofar iron(III) oxide phases is also active in the heterogeneous Fenton oxidation and several chemical and physical effects, including the microstructure, are known to affect their catalytic activity and the underlying catalytic mechanisms [9, 10, 27, 28]. The scope of this paper is to demonstrate the potential of laterites calcined at moderate temperature for the heterogeneous Fenton oxidation and provide new insight into the microstructure-catalytic activity relationships of this catalyst in the degradation of methylene blue as a dye molecule model.

Experimental

Preparation of laterite-based materials

Laterite stone feedstock were collected from a quarry in Dano, a town in the southwest of Burkina Faso, located 60 km from the border of Ghana**.** The laterite stones were crushed and sieved. The fraction smaller than 225 microns named raw laterite (RL) was used for the different tests. Calcination of the raw laterite at different temperature was performed in a furnace with a heating rate of 10 ° C / min and a 2 hours steady stage at the desired temperature, namely 400°C, 600°C and 800°C. Depending on their calcination temperature, the calcined laterites were labeled LT- 400, LT- 600 and LT- 800, respectively.

Characterization of laterite and calcined laterites

Firstly, quantitative analysis of crystalline phases by powder X-ray diffraction and SEM/EDS analysis were performed on the raw laterite in order to thoroughly characterize the pristine laterite material. X-ray diffraction patterns were recorded on a Bruker D8 Vario1 diffractometer, using Cu Kα radiation (λ = 0.154 nm) and equipped with a Lynx Eye detector (detector opening 3.5°). The X-ray generator was set to 40 kVand 40 mA, the recorded angular rangewas 5 to 90° (2θ) with a step close to 0.014°. The quantitative analyses were performed using the Rietveld method with the PANalytical X'Pert HighScore Plus software. EDS (Energy Dispersive X-Ray Spectroscopy) semi-quantitative analyzes were performed on a ZEISS SUPRA 55 scanning electron microscope equipped with an EDS analyzer EDAX. Qualitative X-ray diffraction analysis was then used to investigate the modifications in the laterite microstructure depending on the calcination temperature. To that end, the diffraction patterns were recorded on a Philips X'Pert diffractometer using Cu Kα radiation (λ = 0.154 nm), at a voltage of 40 kV and an intensity of 20 mA. Nitrogen adsorption and desorption isotherms were recorded using a Micromeritics 3Flex Surface Characterization instrument apparatus to characterize the textural properties of the different laterite samples. Brunauer – Emmett - Teller (BET) method was used to assess the specific surface area of the samples. Micropores and mesopores distribution was determined using the DFT model. Thermal gravimetric analysis (TGA) and differential scanning calorimetry (DSC) were performed to investigate the chemical transformations occurring during the calcination of the laterite material. TGA-DSC were conducted on the raw laterite sample under argon atmosphere at a low rate of 100 mL min^{-1} and a

heating rate of 10 °K min^{-1} from 20 to 1100 °C. The pH values at the point of zero charge (pH_{PZC}) of the laterite-based catalysts were measured using the method described by Noh and Schwarz [29]. The pH of a solution of 0.1 M NaCl was adjusted between pH 2 and pH 10 by adding either HCl or NaOH. A total of 0.1 g of the laterite-based catalyst was added to 20 mL of the NaCl solutions. After the pH had stabilized (typically after 24 h under stirring), the final pH was recorded. The graphs of final pH versus initial pH were used to determine the points at which the initial pH was equal to the final pH. This point was taken as the pH_{PZC} of the catalyst.

Adsorption and catalytic experiments

Methylene blue (MB) used in this study was purchased from Reactif RAL. H_2O_2 was obtained from Gilbert Laboratories. A given amount of laterite-based sample was mixed in a MB solution and stirred for 20 minutes in order to reach the MB adsorption equilibrium, as shown in Figure 5. Except for adsorption experiments, a given amount of H_2O_2 solution was then added to the mixture in order to enable the MB Fenton degradation. The stirring speed was 230 rpm for all the experiments. All MB degradation experiments were carried out at room temperature, unless otherwise mentioned. Aliquots were withdrawn from the reactor each 20 minutes for spectrophotometric analysis. Sodium sulfite, a hydroxyl radical quencher, and sodium hydroxide were added to the aliquots in order to stop the Fenton reaction. The concentration of dye in the reaction mixture at different times was obtained by measuring the absorbance at 661 nm and computing the concentration from a calibration curve. A Spectrophotometer DR 5000 was employed for absorbance measurements using quartz cells. The total iron leached at the end of MB removal test was analyzed using Atomic Absorption NovAA 400P Analytik Jena**.** During the study on the influence of light, the test with light was done using the natural radiation in the laboratory room and the test in darkness was carried out by covering the whole surface of the Erlenmeyer flask with aluminum paper. The temperature was set at the desired value with the hot plate and controlled with a thermocouple at begin of the test, and then the plate was kept at this temperature during the test. The initial pH of the MB solutions was adjusted to the desired value using sulfuric acid and sodium hydroxide addition. In order to study homogeneous Fenton contribution in the mechanisms of MB removal, homogeneous Fenton experiments were carried out using ferrous sulfate as the iron precursor at a concentration of 0.12 $mg.L^{-1}$, corresponding to the maximum iron leached concentration value measured by atomic absorption at the end of the heterogeneous catalytic test. The other reaction parameters were similar to the heterogeneous catalytic tests.

Results and discussion

Laterite and calcined laterite characterization

Semi-quantitative EDS Elemental analyses of the raw laterite sample indicate that the main mineral element found in the material are Al, Si, Fe and Ti (Fig. S1 in Supplementary Information and Table 1). From these data, the Rietveld refinement analysis displayed in Figure S2 (Supplementary Information), highlighted that the main crystalline phases are kaolinite ($Si_2O_5Al_2(OH)_4$), which is the major phase with 36.0 wt% and the quartz (SiO_2) with 16.1 wt%. Iron-based phases are the second subset of crystalline phases with mainly goethite (α-FeO(OH)) with 35.2 wt%, hematite (α-Fe_2O_3) with 6.3 wt% among with 3.2 wt% of ferrite (α-Fe). The total mass content of iron in the crystalline part of the raw laterite was estimated to around 30 wt%**.** The third subset crystalline phases are the titania phases in minute amount. The ocher color of the laterite is attributed to the presence of iron oxides phases. It is reported that in laterite

soil, the different mineral phases are not simply mixed in a physical manner but different kinds of association exist between the components [30–36]. The knowledge of these interactions from the specialized geochemical literature has been thoroughly analyzed in order to better understand the complex microstructural framework occurring in this composite natural material. In particular, the association of goethite and kaolinite phases has been reported to form a stable binary system in which kaolinite and goethite interact relatively strongly by (i) electrostatic attraction, surface coordination (between the O atoms of the kaolinite surface and the Fe atoms of the goethite surface), anion ligand exchange (between hydroxyl groups on the goethite surface and negatively charged oxygen functional groups on the kaolinite surface resulting in Al-O-Fe or Si-O-Fe bonds) and hydrogen bonds [34]. Kaolinite is a clay mineral defined as 1:1-type phyllosilicate of chemical formula Al_2O_3 $2SiO_2$. $2H_2O$. Each layer of kaolinite consists of a silica/oxygen tetrahedral sheet and an alumina/oxygen dioctahedral sheet that share a common plane of oxygen atoms. The surface sites of kaolinite are mainly silanol (≡Si–OH) and aluminol (≡Al–OH) groups situated at the edges and at the hydroxyl-terminated planes of the clay lamellae [34]. The kaolinite layers are linked by hydrogen bonding [37]. Moreover, isomorphic substitution of Fe by Al in goethite, along with isomorphic substitution of Al by Fe in kaolinite have been reported to occur in laterite soil materials [30–34]. The amount of structural iron cation located in the octahedral sheet of the kaolinite is highly minor compared to iron in the form of free oxides but iron substituted domains within kaolinite layer could act as nuclei inducing true bonding between the mineral phases [32]. In laterite soil, flaky mineral plates are aggregated into microcrystalline domains that are coated with free iron oxides resulting in the occurrence of larger aggregates similar to individual particle. This “cladding form” of free iron oxides in laterite acts as a cementation agent of the composite material [24]. Especially in goethite-kaolinite association as probably existing in laterite, goethite phase has been reported to stand as a protective coating on the kaolinite surface [34]. Another type of free iron oxides is supposed to occur as individual crystalline particles located into the pores of the material [35]. In laterite, such free iron oxides location probably concerns small discrete hematite particles which are known to be in interaction with goethite but not with kaolinite phase [32]. Quartz is reported to occur as individual particles dispersed in the goethite phase [31]. These literature data were helpful to investigate the microstructure evolution of the laterite arising during calcination from XRD patterns of calcined laterites at different temperature (Fig 1). It is obvious from XRD that the microstructure of laterite is strongly modified during calcination. Up to 400 °C, the kaolinite matrix is partially destroyed due to the loss of structural water and the goethite phase previously in association with the kaolinite lattice transforms into free hematite crystallites. This was supported by the TGA-DSC data depicted in Fig 2. DSC curve shows three endothermic peaks followed by exothermic peaks. The first peak between 60 and 120 °C is assigned to the removal of free water in laterite. The peak in the range between 280 to 320°C, associated with a more significant weight loss, is probabily due to the dehydroxylation of goethite resulting in the formation of hematite (Eq. 1), as reported by other authors for the transformation of pure goethite into hematite [38–40].

$$\mathbf{2\,\alpha - FeOOH \;\rightarrow\; \alpha - Fe_2O_3 + H_2O} \qquad \mathbf{(1)}$$

$$\mathbf{Si_2O_5Al_2(OH)_4 \;\rightarrow\; Al_2O_3Si_2O_7 + 2\,H_2O} \qquad \mathbf{(2)}$$

$$\mathbf{2\,Al_2Si_2O_7 \;\rightarrow\; Si_3Al_4O_{12} + SiO_2} \qquad \mathbf{(3)}$$

From the TGA curve, it can be noticed that the weight loss recorded at this temperature range account for about 3% of the weight loss, which is close to the theoretical stoichiometric weight loss corresponding to the weight of H_2O released by the deshydroxylation of the goethite amount assessed by XRD quantitative analysis (Eq. 1 and Fig. S2 in Supplementary Information). However, goethite phase was detected in the XRD pattern of laterite calcined at 400°C.

This feature can be explained by the occurrence of some amorphous iron oxyhydroxides whose deshydroxylation into hematite arises at temperature less than 350°C as detected by TGA, together with goethite in weak interaction with the kaolinite lattice. The remaining goethite phase together with amorphous iron oxyhydroxides in stronger interaction with the kaolinite layers are probably deshydroxylated simultaneously with kaolinite at higher temperature. Indeed, the endothermic peak around 400 and 580 °C in the DSC curve associated with a weight loss of about 6 wt% (Fig. 2) can be attributed to the dehydroxylation of kaolinite resulting in the formation of a disorder metakaolin phase (Eq. 2) [41–43]. By considering the kaolinite fraction in raw laterite inferred from quantitative XRD analysis, namely 36.0 wt% (Fig. 2), the theoretical stoichiometric weight loss corresponding to the removal of structural water (Eq. 2) through the metakaolinisation process is close to 5 wt%. This lower value can be explained by the occurrence of some alumino-silicate in amorphous state in raw laterite that is not taken into account in the quantitative XRD analysis. The collapse of the kaolinite lattice is clearly evidenced by the XRD pattern of the laterite calcined at 600°C that shows the loss of the kaolinite diffraction peaks. Only the crystal planes of the hematite and the quartz phases were detected (Fig. 1). It can be considered that, in the laterite calcined at 600°C, all the iron oxides are in the form of poorly crystallized nano-sized crystallites of hematite, as suggested by the low intensity of the diffraction peaks of hematite, despite the increasing iron oxide content in the sample due to the loss of structural water.

Table 1 Semi-quantitative EDS elemental analyses of the raw laterite sample on three different areas of a SEM image.

Element (spectral ray)	Al (K)	Si (K)	Fe (K)	Ti (K)
Area 1 (At %)	30.29	21.47	48.24	-
Area 2 (At %)	34.11	28.63	35.91	1.35
Area 3 (At %)	34.59	29.69	34.31	1.42

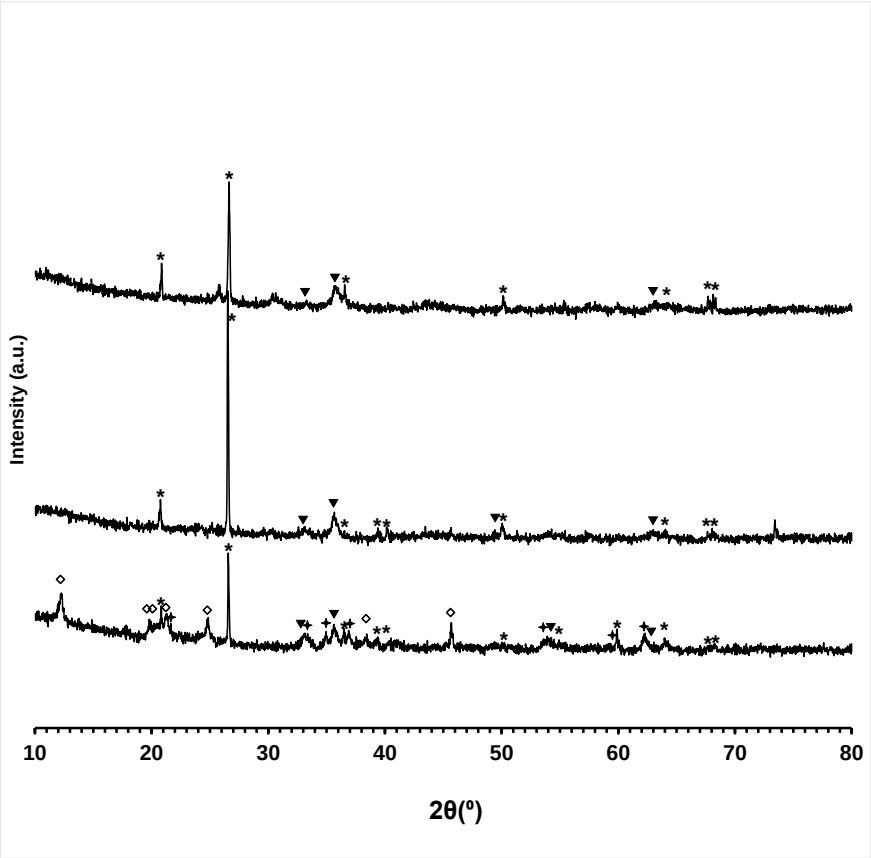

Fig. 1 XRD patterns of calcined laterites. a. LT-400; b. LT-600 and c. LT-800 (◇ Kaolinite, ✦Goethite, ★ Quartz, ▼ Hematite).

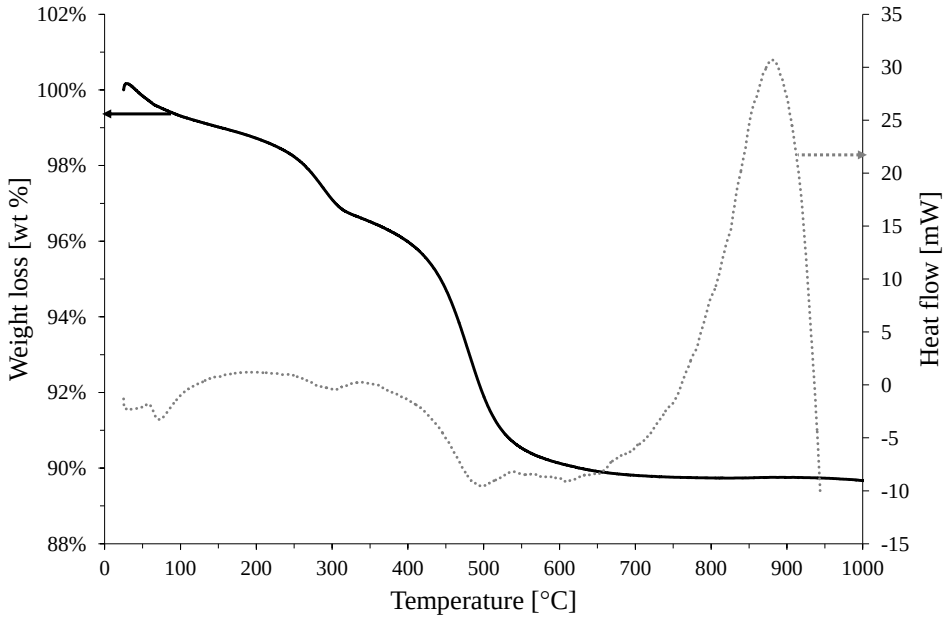

Fig. 2 TGA/DSC analyses of raw laterite

On figure 2, an exothermic peak was observed at around 850 °C and was not associated with any weight loss. This exotherm could be attributed to recrystallisation phenomena resulting in the formation of a spinel phase (Eq. 3) as reported by several authors [25, 44, 45]. The XRD pattern of laterite calcined at 800°C shows the apparition of a new phase in few amount associated with the decrease of the crystallite size of the quartz α (inferred from the Scherrer formula applied to the peak at 26.6°). These features witness of the occurrence of structural modifications during the

calcination treatment from 800°C which match with the begining of the exothermic formation of a spinel phase. The metakaolinisation process has been widely studied and the known phenomena in addition of the de-hydroxylation of kaolinite are the aggregation of the particles of metakaolinite and the beginning of their sintering whose extent depends on the amount of the kaolinite in the natural raw material and the calcination temperature [43].These microstructural modifications result in the global shrinkage of the alumino silicate framework that probably explained the drop of the surface area with the calcination temperature as reported in table 2. The sharp drop of both surface area and pore volume in the laterite calcined at 800°C is in line with the beginning of sintering of metakaolinite particles and formation of a new crystalline phase as detected by XRD. N_2 adsorption desorption isotherms of the raw laterite and the calcined laterites with their associated DFT pore size distribution are depicted in Figures S3 and S4 (Supplementary Information), respectively. All the isotherms are hithermost in shape to type II, characteristic of macroporous or non-porous materials [46]. Nevertheless, a type 3 hysteresis loop was obtained at high relative pressure in the range 0.50–1.00, which is generally attributed to the presence of aggregates of plate-like particles giving rise to slit-shaped mesopores in which N_2 capillary condensation can occur [46]. In raw laterite, these plate-like particles probably consist of staked kaolinite layers covered by free iron oxides as discussed previously. In spite of a poor surface area, the raw laterite exhibits a few extent of micropores as witnessed by the low increase of N_2 adsorption in the relative pressure range of micropore filling. The N_2 adsorption profile (Fig. S3) together with the pore size distribution (Fig. S4) of the calcined laterites depict a gradual loss in microporosity until 600°C which is correlated with the substantial decrease of the surface area (Tab. 2). A sharp drop in surface area, total pore volume and microporosity is observed in the laterite calcined at 800°C. During the metakaolinisation process, the removal of structural water from the kaolinite lattice produces a distortion effect in the 1 : 1 Al–Si layers, which is due to the migration of the aluminium into vacant sites provided by the inter-layer spacing resulting in a reduction of the aluminium coordination within the disordered layers, leading to the aggregation of the metakolinite particles [43, 47]. These structural modifications, accompanied by the dehydroxyation of the goethite protective layers result in an incresingly global shrinkage of the alumino silicate framework with the calcination temperature, and the associated loss of microporosity. Interestingly, it can be noticed from the pore size distribution that until 600°C, the mesoporosity seems to be not affected by the shrinkage effect since a slight increase of the mesopore volume is detected. Actually, the calcination induced shrinkage effect is balanced by the release of structural water from both deshydroxylation of kaolinite and goethite phases leading to the enlargement of the interlayer spacing and the associated mesoporosity. This enhancement of mesopore volume detected for laterites calcined at 400°C and 600°C is of interest for the targeted application as these slit-shape mesopores are supposed to be coated by free iron oxides such as hematite as discussed previously. By contrast, a strong reduction in both micro and mesoporosity arises for the laterite calcined at 800°C, resulting in a sharp drop of the surface area and total pore volume. These textural modifications are associated with the beginning of the sintering of metakaolinite particles and recrystallization phenomena as detected from XRD pattern (Fig. 1).

Table 2 BET Specific area, pore volume and pH_{ZPC} of raw laterite and the calcined laterites.

Laterite-based catalyst	Surface area [$m^2\ g^{-1}$]	Pore volume [$cm^3\ g^{-1}$]	pH_{ZPC}
RL	50	0.103	5.5
TL - 400	36	0.100	5.9
TL - 600	28	0.109	5.5
TL - 800	7	0.047	5.5

Methylene blue adsorption and Fenton oxidation tests

The respective contributions of adsorption and catalytic degradation phenomena during MB removal were investigated on the different laterite-based catalysts. Kinetic data of MB adsorption were obtained from the tests without H_2O_2 addition and are lumped in Table 3. In order to better understand the nature of the MB adsorption on the laterite-based catalysts, electrostatic interactions between the cationic dye and the catalyst surface must be considered. It is known that the protonation of mineral surface is enhanced at pH lower than pH_{ZPC} leading to a net total positive surface charge, while deprotonation is promoted at pH greater than pH_{ZPC} (net total negative surface charge). Surprisingly, all the laterite-based catalysts exhibit similar values of pH_{ZPC} between 5 and 6 (Table 2), which is slightly lower than the values reported for other types of laterites [48, 49]. These values can be considered as combinations of the contribution of high point of zero charge sesquioxides (e.g. goethite and hematite) and low point of zero charge minerals such as kaolinite or quartz [50]. Therefore, under the adsorption tests conditions, all the different laterite-based catalysts in our study have net positively charged surface ($pH< pH_{ZPC}$) leading to unfavorable electrostatic interactions with the cationic MB species. These electrostatic interactions may explain the weak adsorption observed for all the materials that accounts for less than 20% of the initial MB content after 100 min with nearly the same extent for all the laterite samples in spite of their porous textural features as described earlier. Although the induced calcination microstructural modifications do not affect significantly the MB adsorption capacity of the laterite, it is interesting to notice some release of adsorbed MB species occurring after 20 min that increases with the calcination temperature of the laterite while the surface area was decreased. These finding suggest that the MB adsorption over the laterite particles proceeds rather through weak and reversible physical type adsorption than through chemical type adsorption, and mainly occurs on their external surface, the extent of micro- and mesoporosity in the material having no significant effect in the MB adsorption process.

MB removal percentage at t = 100 min from both adsorption and Fenton experiments are compared in Table 3. The comparison of the MB removal experiments without H_2O_2 (adsorption) with those in the presence of H_2O_2 (Fenton degradation) clearly demonstrates that the Fenton reaction is effective. The H_2O_2 addition considerably increased the MB removal rate for all the laterite samples. As demonstrated earlier, the raw laterite and the calcined laterite samples contain significant amount of iron III oxide sites (≡Fe(III)), that are known to enable the heterogeneous Fenton oxidation reactions cycle as described, for instance, by the radical mechanism below (Eq. 4-7) :

$$\equiv Fe(III) + H_2O_2 \rightarrow \equiv Fe(OOH)^{2+} + H^+ \quad (4)$$

$$\equiv Fe(OOH)^{2+} \rightarrow \equiv Fe(II) + HOO^{\circ} \quad (5)$$

$$\equiv Fe(II) + H_2O_2 \rightarrow \equiv Fe(III) + HO^{\circ} + OH^- \quad (6)$$

$$HO^{\circ} + \text{Methylene blue} \rightarrow CO_2 + H_2O + \text{mineralization products} \quad (7)$$

The spectral evolution of the MB solution during adsorption and Fenton oxidation using LT 600 is shown in Figure 3. After 100 minutes of treatment, an almost total disappearance of the peaks located at 291 nm and 661 nm is observed in case of the Fenton oxidation. This disappearance indicates the destruction of the chromophoric groups responsible for the color (np conjugated system) and the UV absorption (aromatic ring). New peaks appeared in UV area (<400 nm) during the Fenton oxidation experiments meanwhile just a small decrease of the MB absorption peaks was observed during the adsorption experiment. These new peaks can be attributed to MB degradation products. Thus, the degradation of the MB molecules during the Fenton oxidation experiment is clearly evidenced.

Table 3 MB removal percentage during adsorption and Fenton oxidation tests using different laterite-based catalysts. Reaction conditions: [Catalyst] = 3 $g.L^{-1}$, $[MB]_0$ = 40 $mg.L^{-1}$, $[H_2O_2]$ = 25 $mg.L^{-1}$ added at t = 20 min, pH = 3, T= 25°C

		Laterite-based catalyst			
	Time [min]	RL	TL-400	TL-600	TL-800
Without H_2O_2	0	0	0	0	0
	20	13.6	23.5	34.4	38.2
	40	13.2	20.1	27.4	32.0
	60	16.8	19.5	25.4	25.2
	80	18.5	18.1	21.9	25.5
	100	18.9	15.7	18.9	18.6
With H_2O_2	100	31.2	94.4	98.9	95.7

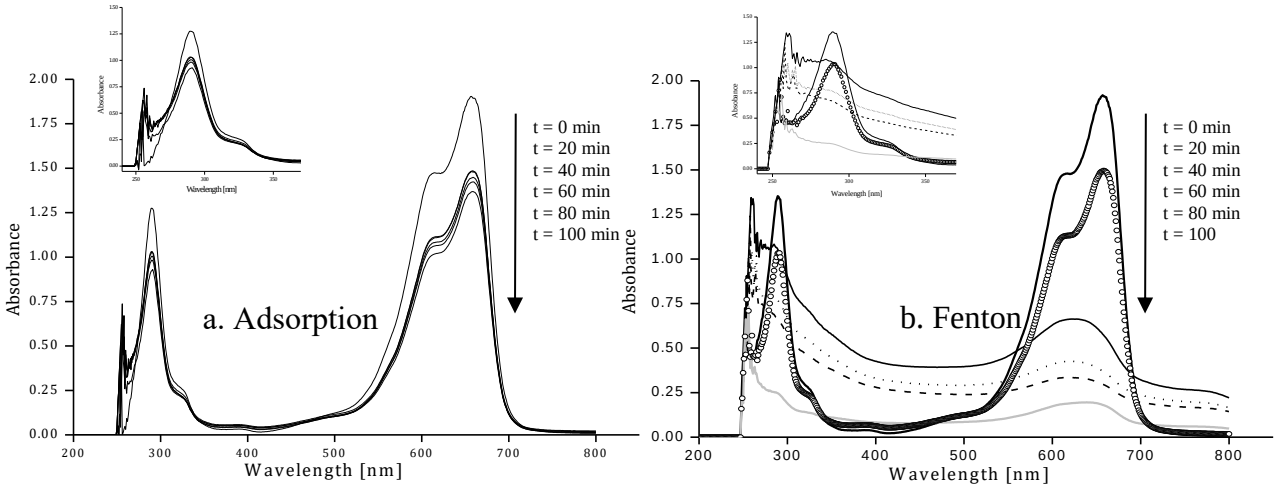

Fig. 3 a. UV-vis absorption spectra during MB adsorption experiment on LT-600 catalyst. Reaction conditions: [Catalyst] = 3 $g.L^{-1}$, $[MB]_0$ = 40 $mg.L^{-1}$, pH = 3, T = 25°C. **b.** UV-vis absorption spectra during MB Fenton degradation experiment using LT-600 catalyst. Reaction conditions: [Catalyst] = 3 $g.L^{-1}$, $[MB]_0$ = 40 $mg.L^{-1}$, $[H_2O_2]$ = 25 $mg.L^{-1}$ added at t = 20 min, pH = 3, T = 25°C.

The MB removal rate in the presence of the laterite calcined at 400°C increased threefold compare to the raw laterite performance and then, increased by 4.5% at 600°C to decrease by 3.2% at 800 °C (Table 3). As demonstrated previously, the calcination strongly modifies the microstructure of the laterite. During calcination up to 400°C, the kaolinite structure is partially destroyed due to loss of structural water and the goethite phase previously in association with the kaolinite lattice transforms into free hematite crystallites, resulting in a drop of the surface area of the composite material due to the shrinkage of the alumino-silicate framework. At 600°C, the kaolinite lattice is further deshydroxylated leading to an amorphous metakaolin matrix containing mainly surface hematite nanophases or poorly crystallized. Besides the transformation of free iron oxides, the calcination is expected to favor the extraction of structural iron from the kaolinite lattice to free iron oxides and thus to increase the accessibility of the iron oxide sites over the catalyst surface. Indeed, similar calcination effect has been already observed in olivine material [51], in natural iron oxide-coated quartzitic aquifer sand [52] or in natural containing iron-clay [53]. Furthermore, it has been reported that in iron-rich kaolinite of soil, pseudomorphic replacement of octahedral Fe^{3+} in the kaolinite lattice by octahedral Al^{3+} is favor by oxidation process and results in the formation of free iron oxides along with silica and alumina residue [54]. Such transformations are expected to occur during the calcination of the raw laterite thus increasing the amount of

free iron oxides available at the surface of the catalyst. Concerning the nature of the iron oxides sites, it has been demonstrated from XRD that goethite is the main iron based phase in the raw laterite but is not any more detected at 600°C. Hematite was also detected but remained as small crystallites or poorly crystallized phase in calcined laterites, while the total Fe_2O_3 amount in the whole material increased with the calcination temperature due to deshydroxylation reaction. Hematite has been reported to achieve the highest activity in catalyzing 2-Chlorophenol oxidation by Fenton process comparatively to goethite, although goethite was more active in the decomposition of H_2O_2 [55]. Furthermore, it has been reported that the crystallinity of hematite particles prevails over the surface area effects in the decomposition of H_2O_2 [56]. These findings reported for pure iron oxides are in accordance with the increase of the Fenton oxidation catalytic performances of the laterite with the calcination temperature and the corresponding microstructure modifications described earlier. It can be retained that the calcination treatment strongly enhances the accessibility of iron oxides and provides hematite nanophases with more catalytically active sites than in the pristine raw laterites. Moreover, the slight increase in the mesoporosity induced by calcination up to 600°C is probably favorable to internal diffusion of MB, H_2O_2 and degradation by-products, thus increasing the whole kinetics of the removal process. The Laterite calcined at 600°C exhibits the highest performance in the presence of H_2O_2 with a degradation rate of 98 % after hundred minutes of treatment at room temperature. The calcination treatment is also expected to improve the catalytic stability of the laterite through the limitation of iron leaching in aqueous solution during the Fenton oxidation experiment, thanks to a reinforcement of the iron oxides clay interactions. The concentrations of iron leached in the solution at the end of the experiment are summarized in Table 4. These values are much lower than the iron concentrations usually used in classical homogeneous Fenton process and to the iron concentration values resulting from iron leaching reported to induce homogeneous Fenton mechanisms [10, 57]. In order to discard some possible homogeneous Fenton contribution in the catalytic degradation performance of our system, homogeneous Fenton experiments were carried out using ferrous sulfate as the iron precursor at a concentration of 0.12 $mg.L^{-1}$, corresponding to the maximum iron leached concentration value measured at the end of the heterogeneous catalytic tests, the other reaction parameters being similar to the heterogeneous catalytic tests. MB removal percentage recorded in these conditions are given in Table 5.

Table 4 Concentration of iron leached in solution after 100 min reaction time.
Reaction conditions: [Catalyst] = 3 $g.L^{-1}$, $[MB]_0$ = 40 $mg.L^{-1}$, $[H_2O_2]$ = 25 $mg.L^{-1}$ added at t = 20 min, pH = 3, T = 25°C

Laterite-based catalyst	RL	TL 400	TL 600	TL 800
Iron concentration [$mg.L^{-1}$]	0.11	0.02	0.12	0.08
Wt/Wi [%][a]	11.3[b]	2.0[b]	11.1[b]	7.4[b]

[a] Wt- total iron weight leached in solution, Wi - initial crystalline iron weight in the catalyst
[b] The value of Wi are estimated based on the iron content in the crystalline phases from the XRD quantitative analysis of the raw laterite and taking into account the weight loss recorded by TGA for the calcined laterite samples

Table 5 MB decolorization percentage during homogeneous Fenton oxidation test.
Reaction conditions: $[Fe^{2+}]$ = 0.12 $mg.L^{-1}$, $[BM]_0$ = 40 $mg.L^{-1}$, $[H_2O_2]$= 25 $mg.L^{-1}$ added at t = 0 min, pH = 3, T= 25°C

Time [min]	0	60	90	150	210
Removal percentage [%]	0	11.6	13.7	15.8	18.3

It appears that in these conditions, the highest contribution of a homogeneous Fenton oxidation process cannot reach more than 15% of MB removal percentage after a reaction time of 100 min, while during this period, the MB removal percentage reached 98% with the TL-600 catalyst used in same condition (Table 3). Therefore, it can be concluded that the MB removal predominantly result from a heterogeneous Fenton mechanism, as described for example by equations

4 to 7. The approximate iron weight loss by leaching has been assessed based on the iron content in the crystalline phases quantified from Rietveld quantitative XRD analysis of the raw laterite and taking into account the weight loss recorded by TGA for the calcined laterite samples (Table 4). These values are obvious approximate, the amorphous material is not taken into account in the XRD quantitative analysis but it provides some useful indications about the extent of iron leaching. Interestingly, the laterite calcined at 400°C exhibits the highest stability towards iron leaching which can be attributed to the strengthen of the iron oxides kaolinite interactions as long as the kaolinite structure was maintained. These issues are under consideration in order to improve the catalyst stability while ensuring an optimum catalyst activity. The laterite calcined at 600°C exhibited the highest catalytic performances after 100 min reaction time and was used for the following experiments.

Effect of reaction conditions on TL-600 catalytic activity

Effect of pH

Optimization of degradation conditions were performed via an evaluation of different reaction parameters. In each test one parameter was changed while the others were held constant. The effect of pH on the MB removal was investigated at a pH range of 2 – 9. The results obtained are summarized in Table 6. The MB removal at pH 3.0 was the most efficient heterogeneous Fenton process. It is well known according to the literature on homogeneous Fenton process that the optimal pH value is 3 due to the formation of less reactive iron species at lower and higher pH values, with the precipitation of $Fe(OH)_3$ at pH higher values than 4 [10]. Interestingly, the LT-600 catalyst exhibits a heterogeneous Fenton activity over a wide range of pH, which is one of the main advantages of heterogeneous processes over the classical Fenton process [58–60]. It is worth remembering that the iron leaching detected with the LT-600 is not quite significant to attribute the removal of MB to a homogeneous process as demonstrated in the previous section. Therefore, the removal of MB has been attributed to the catalytic activity of iron oxides, especially nanophase hematite closely integrated in the laterite structure, as demonstrated earlier. This feature explained the fairly good efficiency at neutral and basic pH. A high MB removal rate (around 90%) was obtained for a wide range of pH (2 to 4.5) and reached 65 % at neutral pH. The decrease of the MB removal rate for pH values higher than 4 may be attributed to a decrease in the production of hydroxyl radicals due to the decomposition of hydrogen peroxide into oxygen (O_2) and water (H_2O), although the occurrence of more favorable electrostatic interactions between the catalyst surface that becomes negatively charged at pH higher than pH_{ZPC}, and the positively charged MB [18, 61].

Table 6 Influence of pH on the MB decolorization by Fenton process using TL-600 after 100 min reaction time. Reaction conditions: $[MB]_0$ = 40 mg.L^{-1}, [Catalyst] = 3 g.L^{-1}, $[H_2O_2]$ = 25 mg.L^{-1} added at t = 20 min, T = 25°C

Initial pH	2	3	4	4.5	7	9
Removal percentage [%]	94.6	98.5	95.2	87.5	65.1	56.9

Effect of temperature

Results on temperature effect on the Fenton degradation of MB are presented on Table 7. In the temperature range studied, the temperature has no influence in the removal of MB by the Fenton process over the laterite LT–600 and the optimum temperature was 25°C. Higher optimum temperatures in the range 50-70°C were reported for Fenton processes using iron-clays [60, 62–64]. The positive temperature effect on the Fenton reaction is balanced by the temperature enhanced thermal decomposition of H_2O_2 into oxygen and water, limiting the Fenton reaction [60, 62–64].

In this study, the heterogenous Fenton LT-600 catalyst / H_2O_2 system exhibited a stable catalytic activity over a wide range of temperature, which is of particular interest if practical operation in hot and sunny environment are contemplated.

Table 7 MB decolorization percentage obtained at different temperatures by Fenton process using TL-600 catalyst after 100 min reaction time. Reaction conditions**:** $[MB]_0$ = 60 mg.L^{-1}, $[H_2O_2]$ = 40 mg.L^{-1} added at t = 20 min, [Catalyst] = 3 g.L^{-1}, pH = 3

Temperatures [°C]	Removal percentage [%]
25	99.4
50	97.7
75	98.5
100	96.1

Effect of initial MB concentration

Figure 4 compared the catalytic performance in various initial MB concentrations from 20 to 100 mg L^{-1}. The MB removal rate at 100 min reaction time was higher than 95% at the initial concentrations from 20 to 60 mg L^{-1}, and then slowed down from values higher than 60 mg L^{-1}. When initial MB concentration increases, the MB adsorption onto the catalyst surface is expected to reach saturation more rapidly and slow down the Fenton degradation process, probably because electron transfer between the catalytic sites and H_2O_2 molecules was intervened by adsorbed MB and/or by-products on the catalyst surface. This adsorption results in a decrease in the number of catalytic active sites in the course of the reaction, and thus gradually damages the catalytic efficiency. Nevertheless, more than 60 % of MB removal is reached for the highest initial concentration of 100 mg L^{-1} which is comprised within the dyes concentration values usually found in textile industry wastewaters ranging from 10 to 250 mg L^{-1} [65]. High concentrated solutions might be efficiently treated by adjusting both the catalyst dosage and the H_2O_2 concentrations, as addressed in the next sections.
In order to obtained kinetics data from this complex heterogeneous Fenton-like mechanism, the experimental results were fitted using an advanced non-linear pseudo-first order model involving the fitting of the apparent rate constant k_{app}, the amplitude A and the endpoint E of the process (Eq. 8) [66].

$$[MB]_t = Ae^{-k_{app}t} + E \qquad (8)$$

The endpoint E of the process is defined as the value of MB concentration at equilibrium infinite time. The amplitude of the process A is linked to the value of E since for t = 0, the initial MB concentration is equal to $A + E$. The fitting of the endpoint is particularly of interest for the modeling of a multi-step complex system compared to the conventional linearization of the equations in a logarithmic form which implies to assume a value for the reaction endpoint. Thus, in the exponential model described in equation 8, the degradation efficiency must be appreciated by considering both the values of k_{app} and E. The fitting was applied from the time of H_2O_2 addition (t = 20 min) when the heterogeneous Fenton reaction is expected to occur. The results of fitting are summarized in Table 8 and highlight the robustness of the model to fit the kinetics data. It is noteworthy that the degradation performance is associated with a high value of k_{app} together with a value of E tending towards 0. When E becomes significant for initial MB concentration higher than 60 mg L^{-1}, the only value of k_{app} is not representative of the catalytic efficiency. The sharp increase of E while the values of

k_{app} do not vary significantly can be explained by the decrease of the number of active sites on the catalyst surface and can be thereby an indicator of the extent of catalyst deactivation by MB and MB by-products adsorption.

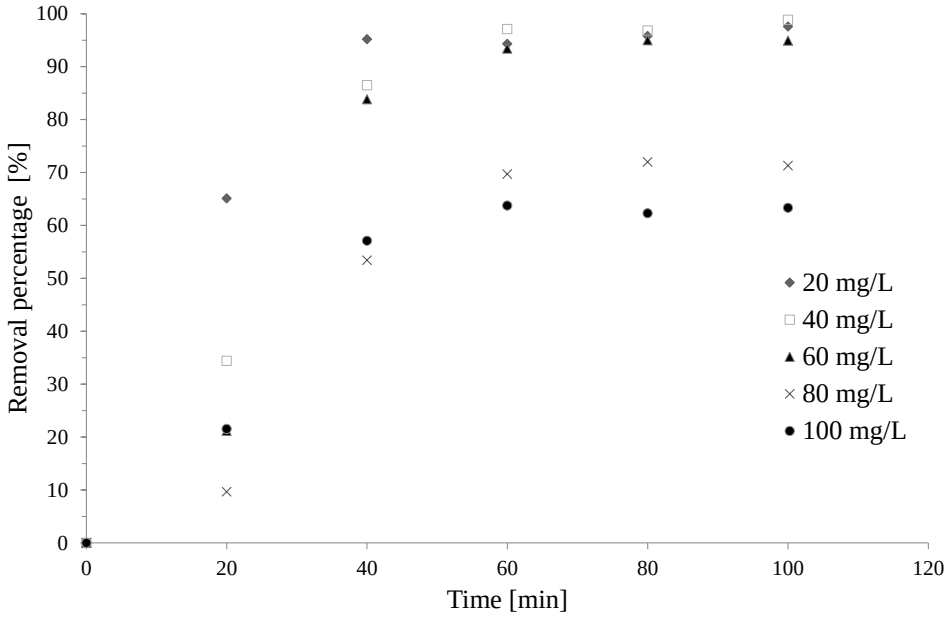

Fig. 4 Influence of initial MB concentration on MB decolorization using LT-600 catalyst. Reaction conditions: $[H_2O_2]$ = 25 mg.L^{-1} added at t = 20 min, [Catalyst] = 3 g.L^{-1}, pH = 3, T = 25°C

Table 8 Effects of initial MB concentration on MB decolorization in 100 minutes using TL-600 catalyst and parameters of pseudo first order kinetic model related to MB concentration. Reaction conditions: [Catalyst] = 3 g.L^{-1}, $[H_2O_2]$ = 25 mg.L^{-1} added at t = 20 min, pH= 3, T = 25°C

BM initial concentration (mg L^{-1})	Removal percentage at t = 100 min [%]	k (min^{-1})		Amplitude (mg L^{-1})		Endpoint (mg L^{-1})		R^2
		Value	SE[a]	Value	SE[a]	Value	SE[a]	
20	97.8	0.180	0.091	6.17	0.31	0.81	0.16	0.9931
40	98.9	0.085	0.005	25.60	0.43	0.64	0.25	0.9992
60	95.0	0.094	0.001	44.36	0.08	2.94	0.05	0.9999
80	71.3	0.061	0.005	50.94	1.57	21.44	1.03	0.9974
100	59.1	0.097	0.009	41.85	1.09	36.63	0.60	0.9981

[a]Standard error for the determined parameters

Effect of H_2O_2 concentration

The concentration of H_2O_2 is a critical parameter in the heterogeneous Fenton reaction. The effect of H_2O_2 concentration on the degradation of MB using LT-600 catalyst is depicted in Figure 5. Only 25 % of MB was adsorbed after 100 minutes on the LT-600 catalyst during the experiment without H_2O_2 and the adsorption equilibrium is already reached at 20 min. The MB efficiency degradation increased obviously with the increase of H_2O_2 concentration from 5 to 40 mg.L^{-1} because of the boost of °OH generated by H_2O_2 over the LT-600 catalyst surface. Nevertheless, the increase of degradation efficiency became decreasingly significant when H_2O_2 concentration increased, because of the so-called scavenging effect of excessive H_2O_2 (Eq. 9) resulting in a reduction of the availability of °OH and thus degradation efficiency, the hydroperoxyl radicals (HOO°) generated being significantly less reactive [10].

$$H_2O_2 + {}^{\circ}OH \rightarrow HOO^{\circ} + H_2O \quad (9)$$

Table 9 summarized the pseudo-first order kinetics parameters showing an actual kinetics improvement with the increase of H_2O_2 concentration and sustains that the previous reaction (Eq. 9) is negligible in the used experimental conditions.

Table 9 Parameters of pseudo first order kinetic model related to MB concentration for different H_2O_2 concentrations using TL-600 catalyst. Reaction conditions: $[MB]_0$ = 60 mg.L^{-1}, [catalyst] = 3 g.L^{-1}, pH = 3, T = 25°C

H_2O_2 concentration (mg L^{-1})	k (min^{-1})		Amplitude (mg L^{-1})		Endpoint (mg L^{-1})		R^2
	Value	SE[a]	Value	SE[a]	Value	SE[a]	
0	0.099	0.035	15.89	1.53	47.89	0.73	0.9652
5	0.091	0.010	21.88	0.71	22.18	0.40	0.9970
10	0.097	0.014	32.40	1.27	12.59	0.70	0.9956
15	0.099	0.001	34.87	0.12	8.91	0.07	1.0000
20	0.079	0.001	41.12	0.09	5.75	0.06	1.0000
25	0.094	0.001	42.71	0.08	2.83	0.04	1.0000
30	0.092	0.002	45.69	0.24	2.48	0.13	1.0000
35	0.106	0.002	43.94	0.24	1.53	0.13	0.9999
40	0.114	0.005	47.52	0.47	0.91	0.25	0.9997

[a]Standard error for the determined parameters

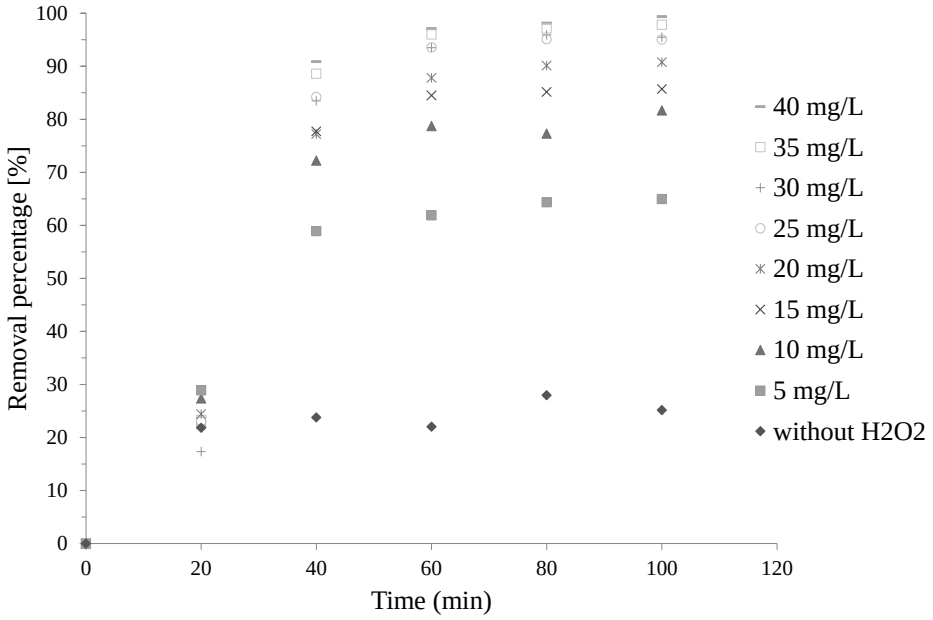

Fig. 5 Influence of H_2O_2 concentration on MB decolorization using LT-600 catalyst Reaction conditions: $[MB]_0$ = 60 mg.L-1, [Catalyst] = 3 g.L^{-1}, pH = 3, T = 25°C

Effect of catalyst dosage

Figure 6 depicts the influence of the catalyst dosage on the removal of MB. The experiment performed in the presence of H_2O_2 and without catalyst resulted in nearly no MB removal which confirm that H_2O_2 itself cannot oxidize MB. During the adsorption stage in the first 20 minutes, the MB removal rate increases with the dosage of LT-600

catalyst because of the increase of the adsorption sites. After the addition of H_2O_2, the MB removal rate increased from 91 to 99% when the concentration of the catalyst was increased from 1 to 3 g L^{-1}. A higher degradation efficiency was observed as the catalyst dosages were increased, due to the increase of the catalytic active sites on the surface of the catalyst and the associated generated free hydroxyl radicals (Eq. 4-6). Surprisingly, the degradation efficiency was impaired when the catalyst dosage was further increased from 3 to 5 g L^{-1} (Fig. 6). The highest kinetic constant of heterogeneous Fenton reaction over the LT–600 catalyst was achieved at 3 g L^{-1} of catalyst dosage and then decreased for higher values, with a concomitant increase of the reaction endpoint (Table 10). This phenomenon has been already observed in other heterogeneous Fenton systems and is attributed to scavenging effect of °OH radicals during unwanted side reactions over the catalyst surface (Eq. 10-12) [12, 67]. Therefore, the increase of catalyst dosage should be accompagnied by an increase in H_2O_2 concentration and an optimum concentrations ratio has to be maintained.

$$\equiv \mathbf{Fe(II)} + \mathbf{^\circ OH} \rightarrow \equiv \mathbf{Fe(III)} + \mathbf{OH^-} \quad \textbf{(10)}$$

$$\equiv \mathbf{Fe(III)} + \mathbf{^\circ OOH} \rightarrow \equiv \mathbf{Fe(II)} + \mathbf{O_2} + \mathbf{H^+} \quad \textbf{(11)}$$

$$\equiv \mathbf{Fe(II)} + \mathbf{^\circ OOH} \rightarrow \equiv \mathbf{Fe(III)} + \mathbf{HOO^-} \quad \textbf{(12)}$$

Table 10 Parameters of pseudo first order kinetic models related to MB at different catalyst dosage using TL-600 catalyst. Reaction Conditions: [H_2O_2] = 25 mg.L^{-1} added at t = 20 min, pH = 3, T = 25°C

Catalyst dosage (g L^{-1})	k (min^{-1})		Amplitude (mg L^{-1})		Endpoint (mg L^{-1})		R^2
	Value	SE[a]	Value	SE[a]	Value	SE[a]	
1	0.034	0.001	52.68	0.34	1.64	0.31	0.9999
2	0.041	0.002	47.31	0.21	1.46	0.74	0.9992
3	0.117	0.002	47.31	0.21	1.12	0.11	0.9999
4	0.087	0.006	44.06	0.93	2.57	0.53	0.9987
5	0.044	0.005	31.99	1.46	5.70	1.16	0.9950

[a]Standard error for the determined parameters

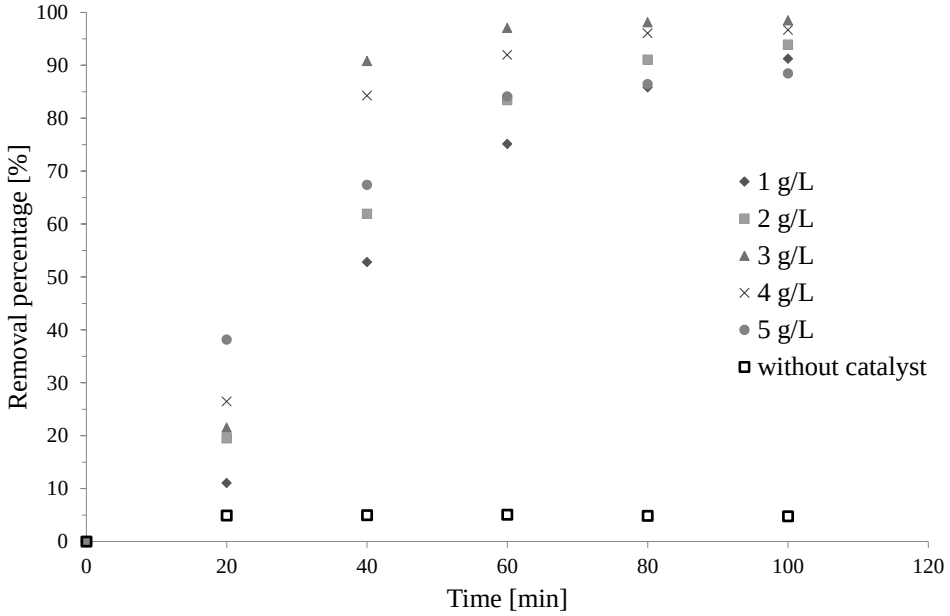

Fig. 6 Influence of catalyst dosage on MB decolorization using LT-600 catalyst
Reaction conditions: $[MB]_0$ = 60 mg.L^{-1}, [H_2O_2] = 40 mg.L^{-1} added at t = 20 min, pH = 3, T = 25°C

Effect of natural light irradiation

The impact of natural light irradiation on the degradation of MB has been investigated. Figure 7 evidences the positive influence of natural light irradiation on the MB degradation reaction over the LT-600 catalyst, since the same experiment performed in darkness resulted in almost the same effect than a two-fold reduction of the H_2O_2 concentration. It is well known that UV/visible irradiation accelerates both Fenton (H_2O_2/Fe^{2+}) and Fenton-like (H_2O_2/Fe^{3+}) reactions, improving the degradation rates of various dyes [57, 68–72]. In photo-Fenton systems, the generation of radicals by two main photo-assisted mechanisms is expected to occur under light irradiation: i) direct photolysis of H_2O_2 (Eq. 13) and ii) photo-reduction of the Fe^{3+} or its $Fe(OH)^{2+}$ complexes into Fe^{2+} (Eq. 14 and 15) allowing the subsequent Fenton reaction (Eq. 16) .

$$\mathbf{H_2O_2} + h\upsilon \rightarrow \mathbf{^{\circ}OH} + \mathbf{^{\circ}OH} \quad (5)$$

$$\mathbf{Fe^{3+}} + h\upsilon + \mathbf{H_2O} \rightarrow \mathbf{Fe^{2+}} + \mathbf{H^{+}} + \mathbf{^{\circ}OH} \quad (6)$$

$$\mathbf{Fe(OH)^{2+}} + h\upsilon \rightarrow \mathbf{Fe^{2+}} + \mathbf{^{\circ}OH} \quad (7)$$

$$\mathbf{Fe^{2+}} + \mathbf{H_2O_2} \rightarrow \mathbf{Fe^{3+}} + \mathbf{OH^{-}} + \mathbf{^{\circ}OH} \quad (8)$$

However, the photo-chemically active region of photo-activation of H_2O_2 lies in the UV-C region (230-290 nm) whereas the solar radiation reaching the earth's surface is exempt of UV-C radiation due to their absorption by oxygen and ozone in the stratosphere [73–75]. On the other hand, the photo-Fenton reactions (Eq. 14 and 15) where Fe^{3+} ion or its $Fe(OH)^{2+}$ complexes act as light absorbing species, producing hydroxyl radicals while the initial Fe^{2+} ion is regained, use irradiation in the UV-visible region up to a wavelength of 600 nm and thus occur under solar light irradation [76, 77]. However, in the present study, the iron species detected in solution were not sufficient to consider a significant homogeneous Fenton mechanism contribution as discussed earlier. Therefore, the slight natural light irradiation induced removal enhancement effect observed in Figure 7, can be attributed to the photocatalytic activity of the hematite nanophases present at the surface of the LT-600 catalyst. Indeed, hematite is a well-known semiconductor with a band gap of 1.9-2.2 eV that can be activated by illumination with visible region in the solar spectrum [73, 78]. Upon solar light excitation, an electron from the α-Fe_2O_3 is promoted from the valence band to the conduction band (e_{CB}^-), leaving a hole in the valence band (h_{VB}^+) (Eq. 17). The e_{CB}^- and h_{VB}^+ are subsequently transformed into reactive hydroxyl radical and superoxide radical anion, contributing to the degradation of the organic molecules (Eq. 18-19).

$$\mathbf{\alpha Fe_2O_3} + h\upsilon \rightarrow \mathbf{\alpha Fe_2O_3}\,(\boldsymbol{e^- + h^+}) \quad (9)$$

$$\mathbf{\alpha Fe_2O_3}\,(\boldsymbol{h^+}) + \boldsymbol{OH^-_{ads}} \rightarrow \mathbf{\alpha Fe_2O_3} + \mathbf{^{\circ}OH_{ads}} + \quad (10)$$

$$\mathbf{\alpha Fe_2O_3}\,(\boldsymbol{e^-}) + \mathbf{O_2} \rightarrow \mathbf{\alpha Fe_2O_3} + \mathbf{^{\circ}O_2^-} \quad (11)$$

This finding is of particular interest in view of practical applications of the use of widely available laterites in the Sub-Saharan African region that receives about 2500–3000 h of solar radiation annually with more than 2000 kWh m^{-2} an^{-1} irradiance in the most parts [79, 80]. Therefore, improved photocatalytic performances are expected for the LT-600 catalyst under actual solar light irradiation.

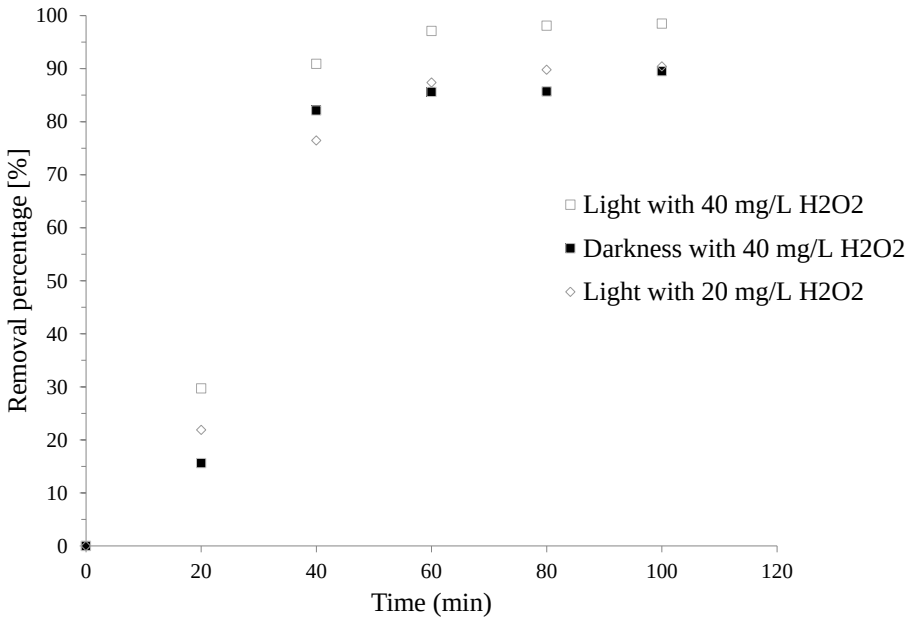

Fig. 7 Influence of natural light on MB decolorization using LT-600 catalyst**.** Reaction conditions: [Catalyst] = 3 $g.L^{-1}$, $[MB]_0$ = 60 $mg.L^{-1}$, $[H_2O_2]$ = 40 $mg.L^{-1}$ added at t = 20 min, T = 25°C, pH = 3

Catalyst reutilization

One of the important qualities of a catalyst is its ability to be reused. Two types of experiments were performed to assess the potential of the LT-600 catalyst reutilization. In a first experiment the lateritic catalyst was washed five times with distilled water before its reuse in another experiment (Fig. 8). After four cycles, the MB removal rate was decreased from 99.4 % to 75% after 100 min reaction time. Moreover, a drop in MB removal of 20 % observed during the first 20 minutes, before the addition of H_2O_2 witnesses a decrease in the catalyst adsorption capacity. In the second experiment, the catalyst was washed and dried at 50 °C, then used in a second cycle (Fig. 8, empty triangle points). The drying step in the recycling process turned out to be detrimental to the degradation performances of the catalyst and might be attributed to poisoning of iron oxide catalytic sites by MB degradation by-products during the drying step in addition of the poisoning effect in the liquid phase during the Fenton reaction. In both experiments, a decrease of adsorption and Fenton oxidation capacities is observed. The difficulty in completely removing the MB degradation by-products from the catalyst surface along with catalyst losses occurring during the recovering step may be considered as the reason for this decrease of activity, as reported elsewhere [60, 63]. Although an efficient regeneration process of the catalyst has yet to be developped, the LT-600 catalyst turned out to keep high degradation efficiency over four subsequent cycles and thus demonstrated its potential as a promising candidate for sustained practical applications.

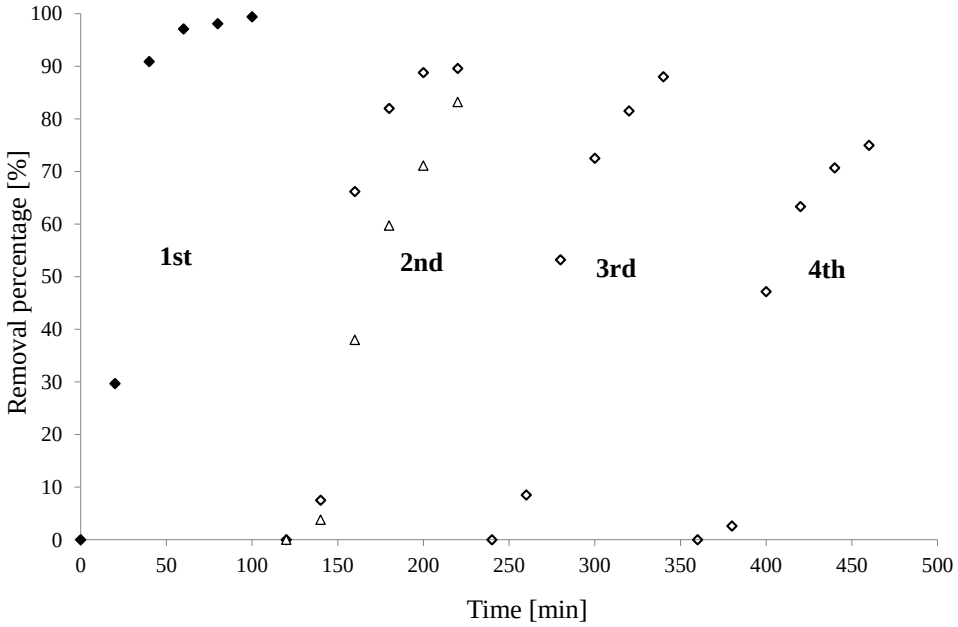

Fig. 8 Reutilization of TL-600 catalyst over several cycles. ◇ Reutilization after washing; △ Reutilization after washing and drying. Reaction conditions: $[MB]_0$ = 60 mg.L^{-1}, $[H_2O_2]$ = 40 mg.L^{-1}, $[Catalyst]_0$ = 3 g.L^{-1}, pH = 3, T = 25 °C

Concluding remarks

In this work, natural laterites from Burkina Faso were calcined at different temperatures in the range 400-800°C and investigated as heterogeneous Fenton catalysts for methylene blue removal. XRD, EDS, N_2 adsorption manometry and TGA-DSC analyses together with thorough analysis of available literature data allowed a finer understanding of the microstructure evolution of the laterite occurring during calcination. Laterite sample consists mainly of goethite and hematite embedded in a framework of kaolinite and quartz with different interaction extents. During calcination up to 400°C, the kaolinite structure is partially destroyed and the goethite phase previously in association with the kaolinite lattice transforms into free hematite crystallites, resulting in a drop of the surface area of the composite material. At 600 °C, the kaolinite lattice is further deshydroxylated leading to an amorphous meta kaolin matrix containing mainly surface hematite nanophases. Besides a strong reduction of the surface area due to the calcination-induced alumino-silica framework contraction, the laterite calcined at 600°C exhibits the highest performance in the methylene blue (MB) degradation by an actual heterogeneous Fenton process with a degradation rate of 99 % after 100 minutes of treatment at room temperature. The effects of solution pH, H_2O_2 concentration, initial MB concentration and catalyst dosage were investigated. A slight but significant visible light induced removal enhancement effect suggested a visible photocatalytic activity of the hematite phase. The calcined laterite demonstrates a strong catalytic stability over several utilizations with a 20 % decrease of the MB removal rate after reuse for four consecutive cycles. Based on these catalytic performances, widely available natural laterites are worth to be seriously considered in the design of sustainable and readily affordable wastewater treatment solutions in developing tropical countries.

References

1. Carmen Z, Daniela S (2012) Textile organic dyes–characteristics, polluting effects and separation/elimination procedures from industrial effluents–a critical overview. In: Organic pollutants ten years after the Stockholm convention-environmental and analytical update. InTech

2. Chergui S (2010) Dégradation des colorants textiles par procédés d'oxydation avancée basée sur la réaction de Fenton: application à la dépollution des rejets industriels. Université Paris-Est

3. Tir M, Moulai-Mostefa N, Nedjhioui M (2015) Optimizing decolorization of methylene blue dye by electrocoagulation using Taguchi approach. Desalination Water Treat 55:2705–2710

4. Karim A Asmaa ;Mounir, Badia ;Hachkar, Mohsine ;Bakasse, Mina ;Yaacoubi (2010) Élimination du colorant basique « Bleu de Méthylène » en solution aqueuse par l'argile de Safi. Rev Sci Eau 23:375–388 . doi: doi:10.7202/045099ar

5. Karthikeyan S, Titus A, Gnanamani A, et al (2011) Treatment of textile wastewater by homogeneous and heterogeneous Fenton oxidation processes. Desalination 281:438–445 . doi: 10.1016/j.desal.2011.08.019

6. Trapido M, Tenno T, Goi A, et al (2017) Bio-recalcitrant pollutants removal from wastewater with combination of the Fenton treatment and biological oxidation. J Water Process Eng 16:277–282

7. Pliego G, Zazo JA, Garcia-Muñoz P, et al (2015) Trends in the Intensification of the Fenton Process for Wastewater Treatment: An Overview. Crit Rev Environ Sci Technol 45:2611–2692 . doi: 10.1080/10643389.2015.1025646

8. Nidheesh PV (2015) Heterogeneous Fenton catalysts for the abatement of organic pollutants from aqueous solution: a review. RSC Adv 5:40552–40577 . doi: 10.1039/C5RA02023A

9. Garrido-Ramírez EG, Theng BK., Mora ML (2010) Clays and oxide minerals as catalysts and nanocatalysts in Fenton-like reactions — A review. Appl Clay Sci 47:182–192 . doi: 10.1016/j.clay.2009.11.044

10. He J, Yang X, Men B, Wang D (2016) Interfacial mechanisms of heterogeneous Fenton reactions catalyzed by iron-based materials: A review. J Environ Sci 39:97–109 . doi: https://doi.org/10.1016/j.jes.2015.12.003

11. Kong S-H, Watts RJ, Choi J-H (1998) Treatment of petroleum-contaminated soils using iron mineral catalyzed hydrogen peroxide. Chemosphere 37:1473–1482 . doi: 10.1016/S0045-6535(98)00137-4

12. Navalon S, Alvaro M, Garcia H (2010) Heterogeneous Fenton catalysts based on clays, silicas and zeolites. Appl Catal B Environ 99:1–26 . doi: 10.1016/j.apcatb.2010.07.006

13. Herney-Ramirez J, Vicente MA, Madeira LM (2010) Heterogeneous photo-Fenton oxidation with pillared clay-based catalysts for wastewater treatment: A review. Appl Catal B Environ 98:10–26 . doi: https://doi.org/10.1016/j.apcatb.2010.05.004

14. Matta R, Hanna K, Chiron S (2007) Fenton-like oxidation of 2,4,6-trinitrotoluene using different iron minerals. Sci Total Environ 385:242–251 . doi: 10.1016/j.scitotenv.2007.06.030

15. Djeffal L, Abderrahmane S, Benzina M, et al (2014) Efficient degradation of phenol using natural clay as heterogeneous Fenton-like catalyst. Environ Sci Pollut Res 21:3331–3338

16. Manu B, Mahamood (2011) Degradation of Paracetamol in Aqueous Solution by Fenton Oxidation and Photo-Fenton Oxidation Processes using Iron from Laterite Soil as Catalyst. Int J Earth Sci Eng 4:1103–1110

17. Karale R, Manu B, Shrihari S (2013) Catalytic use of laterite iron for degradation of 2-aminopyridine using advanced oxidation processes. Int J Sci Eng Res 4:207–210

18. Khataee AR, Pakdehi SG (2014) Removal of sodium azide from aqueous solution by Fenton-like process using natural laterite as a heterogeneous catalyst: Kinetic modeling based on nonlinear regression analysis. J Taiwan Inst Chem Eng 45:2664–2672 . doi: 10.1016/j.jtice.2014.08.007

19. Khataee A, Salahpour F, Fathinia M, et al (2015) Iron rich laterite soil with mesoporous structure for heterogeneous Fenton-like degradation of an azo dye under visible light. J Ind Eng Chem 26:129–135 . doi: 10.1016/j.jiec.2014.11.024

20. Koottatep T, Phong VHN, Chapagain SK, et al (2017) Potential of Laterite Soil Coupling Fenton Reaction in Acetaminophen (ACT) Removal in Constructed Wetlands. Water Air Soil Pollut 228:283 . doi: 10.1007/s11270-017-3454-x

21. Sangami S, Manu B (2017) Synthesis of Green Iron Nanoparticles using Laterite and their application as a Fenton-like catalyst for the degradation of herbicide Ametryn in water. Environ Technol Innov 8:150–163 . doi: https://doi.org/10.1016/j.eti.2017.06.003

22. Tardy Y (1992) Diversity and terminology of lateritic profiles. Weather Soils Paleosols 379–405

23. Nahon D (2003) Altérations dans la zone tropicale. Signification à travers les mécanismes anciens et/ou encore actuels. Comptes Rendus Geosci 335:1109–1119

24. Zhang L, Hong S, He J, et al (2011) Adsorption characteristic studies of phosphorus onto laterite. Desalination Water Treat 25:98–105 . doi: 10.5004/dwt.2011.1871

25. Kenda ES, Py X, N'Tsoukpoe KE, et al (2017) Thermal Energy Storage Materials Made of Natural and Recycled Resources for CSP in West Africa. Waste Biomass Valorization 1–15

26. Munoz M, Pedro ZM de, Casas JA, Rodriguez JJ (2015) Preparation of magnetite-based catalysts and their application in heterogeneous Fenton oxidation – A review. Appl Catal B Environ 176–177:249–265 . doi: https://doi.org/10.1016/j.apcatb.2015.04.003

27. Pouran SR, Abdul Raman AA, Wan Daud WMA (2014) Review on the application of modified iron oxides as heterogeneous catalysts in Fenton reactions. J Clean Prod 64:24–35 . doi: 10.1016/j.jclepro.2013.09.013

28. Liu Y, Jin W, Zhao Y, et al (2017) Enhanced catalytic degradation of methylene blue by α-Fe2O3/graphene oxide via heterogeneous photo-Fenton reactions. Appl Catal B Environ 206:642–652 . doi: https://doi.org/10.1016/j.apcatb.2017.01.075

29. Noh JS, Schwarz JA (1989) Estimation of the point of zero charge of simple oxides by mass titration. J Colloid Interface Sci 130:157–164 . doi: https://doi.org/10.1016/0021-9797(89)90086-6

30. Herbillon A, Mestdagh M, Vielvoye L, Derouane E (1976) Iron in Kaolinite with Special Reference to Kaolinite from Tropical Soils. Clay Miner 11:201–220

31. Mendelovici E, Yariv S, Villalba R (1979) Iron-bearing kaolinite in Venezuelan laterites: I. Infrared Spectrosc Chem Dissolution Evid Clay Miner 14:323–331

32. Boudeulle M, Muller J-P (1988) Structural characteristics of hematite and goethite and their relationships with kaolinite in a laterite from Cameroon: a TEM study. Bull Minéralogie 111:149–166

33. Trolard F, Tardy Y (1989) A model of Fe3+-kaolinite, Al3+-goethite, Al3+-hematite equilibria in laterites. Clay Miner 24:1–21

34. Wei S, Tan W, Zhao W, et al (2012) Microstructure, interaction mechanisms, and stability of binary systems containing goethite and kaolinite. Soil Sci Soc Am J 76:389–398

35. Zhang X, Kong L, Cui X, Yin S (2016) Occurrence characteristics of free iron oxides in soil microstructure: evidence from XRD, SEM and EDS. Bull Eng Geol Environ 75:1493–1503

36. Giovannini AL, Neto ACB, Porto CG, et al (2017) Mineralogy and geochemistry of laterites from the Morro dos Seis Lagos Nb (Ti, REE) deposit (Amazonas, Brazil). Ore Geol Rev 88:461–480 . doi: https://doi.org/10.1016/j.oregeorev.2017.05.008

37. Tan D, Yuan P, Annabi-Bergaya F, et al (2015) Methoxy-modified kaolinite as a novel carrier for high-capacity loading and controlled-release of the herbicide amitrole. Sci Rep 5:8870

38. Fan H, Song B, Li Q (2006) Thermal behavior of goethite during transformation to hematite. Mater Chem Phys 98:148–153

39. Liu H, Chen T, Zou X, et al (2013) Thermal treatment of natural goethite: Thermal transformation and physical properties. Thermochim Acta 568:115–121

40. Guo X, Li D, Park K-H, et al (2009) Leaching behavior of metals from a limonitic nickel laterite using a sulfation–roasting–leaching process. Hydrometallurgy 99:144–150 . doi: 10.1016/j.hydromet.2009.07.012

41. Mitra G t, Bhattacherjee S (1970) X-ray diffraction studies on the transformation of kaolinite into metakaolin. II. Study of layer shift. Acta Crystallogr B 26:2124–2128

42. Maubec N (2010) Approche multi-échelle du traitement des sols à la chaux-Etudes des interactions avec les argiles. Université de Nantes

43. Fabbri B, Gualtieri S, Leonardi C (2013) Modifications induced by the thermal treatment of kaolin and determination of reactivity of metakaolin. Appl Clay Sci 73:2–10 . doi: https://doi.org/10.1016/j.clay.2012.09.019

44. Sonuparlak B, Sarikaya M, Aksay IA (1987) Spinel Phase Formation During the 980° C Exothermic Reaction in the Kaolinite-to-Mullite Reaction Series. J Am Ceram Soc 70:837–842

45. Lu J, Liu S, Shangguan J, et al (2013) The effect of sodium sulphate on the hydrogen reduction process of nickel laterite ore. Miner Eng 49:154–164 . doi: 10.1016/j.mineng.2013.05.023

46. Sing KS (1985) Reporting physisorption data for gas/solid systems with special reference to the determination of surface area and porosity (Recommendations 1984). Pure Appl Chem 57:603–619

47. Sperinck S, Raiteri P, Marks N, Wright K (2011) Dehydroxylation of kaolinite to metakaolin-a molecular dynamics study. J Mater Chem 21:2118–2125 . doi: 10.1039/C0JM01748E

48. Chatterjee S, De S (2016) Application of novel, low-cost, laterite-based adsorbent for removal of lead from water: Equilibrium, kinetic and thermodynamic studies. J Environ Sci Health Part A 51:193–203 . doi: 10.1080/10934529.2015.1094321

49. Maji SK, Pal A, Pal T (2007) Arsenic removal from aqueous solutions by adsorption on laterite soil. J Environ Sci Health Part A 42:453–462

50. Appel C, Ma LQ, Rhue RD, Kennelley E (2003) Point of zero charge determination in soils and minerals via traditional methods and detection of electroacoustic mobility. Geoderma 113:77–93 . doi: https://doi.org/10.1016/S0016-7061(02)00316-6

51. Courson C, Udron L, Świerczyński D, et al (2002) Hydrogen production from biomass gasification on nickel catalysts: Tests for dry reforming of methane. Catal Today 76:75–86 . doi: https://doi.org/10.1016/S0920-5861(02)00202-X

52. Kwan WP, Voelker BM (2003) Rates of hydroxyl radical generation and organic compound oxidation in mineral-catalyzed Fenton-like systems. Environ Sci Technol 37:1150–1158

53. Ausavasukhi A, Sooknoi T (2014) Catalytic activity enhancement by thermal treatment and re-swelling process of natural containing iron-clay for Fenton oxidation. J Colloid Interface Sci 436:37–40 . doi: 10.1016/j.jcis.2014.08.028

54. Rozenson I, Spiro B, Zak I (1982) Transformation of iron-bearing kaolinite to iron-free kaolinite, goethite, and hematite. Clays Clay Miner 30:

55. Huang H-H, Lu M-C, Chen J-N (2001) Catalytic Decomposition of Hydrogen Peroxide and 2-chlorophenol with iron oxides. Water Res 35:2291–2299 . doi: 10.1016/S0043-1354(00)00496-6

56. Hermanek M, Zboril R, Medrik I, et al (2007) Catalytic efficiency of iron (III) oxides in decomposition of hydrogen peroxide: competition between the surface area and crystallinity of nanoparticles. J Am Chem Soc 129:10929–10936

57. Hsueh CL, Huang YH, Wang CC, Chen CY (2005) Degradation of azo dyes using low iron concentration of Fenton and Fenton-like system. Chemosphere 58:1409–1414 . doi: 10.1016/j.chemosphere.2004.09.091

58. Mammeri L, Sehili T, Remache W, Belaidi S (2014) Natural iron oxide as a heterogeneous photo-Fenton-like catalyst for the degradation of 1-naphthol under artificial and solar light. Sci Technol A 91–97

59. Tabet D, Saidi M, Houari M, et al (2006) Fe-pillared clay as a Fenton-type heterogeneous catalyst for cinnamic acid degradation. J Environ Manage 80:342–346 . doi: 10.1016/j.jenvman.2005.10.003

60. Catrinescu C, Teodosiu C, Macoveanu M, et al (2003) Catalytic wet peroxide oxidation of phenol over Fe-exchanged pillared beidellite. Water Res 37:1154–1160 . doi: 10.1016/S0043-1354(02)00449-9

61. Ghanizadeh G, Asgari G (2011) Adsorption kinetics and isotherm of methylene blue and its removal from aqueous solution using bone charcoal. React Kinet Mech Catal 102:127–142 . doi: 10.1007/s11144-010-0247-2

62. Azmi NHM, Vadivelu VM, Hameed BH (2014) Iron-clay as a reusable heterogeneous Fenton-like catalyst for decolorization of Acid Green 25. Desalination Water Treat 52:5583–5593 . doi: 10.1080/19443994.2013.814009

63. Ramirez JH, Costa CA, Madeira LM, et al (2007) Fenton-like oxidation of Orange II solutions using heterogeneous catalysts based on saponite clay. Appl Catal B Environ 71:44–56 . doi: 10.1016/j.apcatb.2006.08.012

64. Khankhasaeva ST, Dambueva DV, Dashinamzhilova ET, et al (2015) Fenton degradation of sulfanilamide in the presence of Al,Fe-pillared clay: Catalytic behavior and identification of the intermediates. J Hazard Mater 293:21–29 . doi: 10.1016/j.jhazmat.2015.03.038

65. Liu G, Zhou J, Wang J, et al (2015) Reductive Decolorization of Azo Dye by Bacteria. In: Singh NS (ed) Microbial Degradation of Synthetic Dyes in Wastewaters. Springer International Publishing, Cham, pp 111–133

66. Lente G (2015) Deterministic kinetics in chemistry and systems biology: the dynamics of complex reaction networks. Springer

67. Ahmed Y, Yaakob Z, Akhtar P (2016) Degradation and mineralization of methylene blue using a heterogeneous photo-Fenton catalyst under visible and solar light irradiation. Catal Sci Technol 6:1222–1232 . doi: 10.1039/C5CY01494H

68. Xu X-R, Li H-B, Wang W-H, Gu J-D (2004) Degradation of dyes in aqueous solutions by the Fenton process. Chemosphere 57:595–600 . doi: https://doi.org/10.1016/j.chemosphere.2004.07.030

69. Scheeren CW, Paniz JNG, Martins AF (2002) Comparison of advanced processes on the oxidation of acid orange 7 dye. J Environ Sci Health Part A 37:1253–1261

70. Liao C-H, Kang S-F, Hung H-P (1999) Simultaneous removal of cod and color from dye manufacturing process wastewater using Photo-Fenton oxidation process. J Environ Sci Health Part A 34:989–1012

71. Lucas MS, Peres JA (2007) Degradation of Reactive Black 5 by Fenton/UV-C and ferrioxalate/H 2 O 2/solar light processes. Dyes Pigments 74:622–629

72. Grčić I, Papić S, Žižek K, Koprivanac N (2012) Zero-valent iron (ZVI) Fenton oxidation of reactive dye wastewater under UV-C and solar irradiation. Chem Eng J 195–196:77–90 . doi: 10.1016/j.cej.2012.04.093

73. Feng J, Hu X, Yue PL (2004) Discoloration and Mineralization of Orange II Using Different Heterogeneous Catalysts Containing Fe: A Comparative Study. Environ Sci Technol 38:5773–5778 . doi: 10.1021/es049811j

74. Tekbaş M, Yatmaz HC, Bektaş N (2008) Heterogeneous photo-Fenton oxidation of reactive azo dye solutions using iron exchanged zeolite as a catalyst. Microporous Mesoporous Mater 115:594–602 . doi: 10.1016/j.micromeso.2008.03.001

75. Komtchou S, Dirany A, Drogui P, et al (2017) Removal of atrazine and its by-products from water using electrochemical advanced oxidation processes. Water Res 125:91–103 . doi: https://doi.org/10.1016/j.watres.2017.08.036

76. Legrini O, Oliveros E, Braun AM (1993) Photochemical processes for water treatment. Chem Rev 93:671–698 . doi: 10.1021/cr00018a003

77. Malato S, Fernández-Ibáñez P, Maldonado MI, et al (2009) Decontamination and disinfection of water by solar photocatalysis: Recent overview and trends. Catal Today 147:1–59 . doi: https://doi.org/10.1016/j.cattod.2009.06.018

78. Cao Z, Qin M, Jia B, et al (2017) Facile synthesis of mesoporous hematite/carbon nanosheet for superior photodegradation. J Phys Chem Solids 107:42–49 . doi: https://doi.org/10.1016/j.jpcs.2017.02.017

79. Ndounla J, Spuhler D, Kenfack S, et al (2013) Inactivation by solar photo-Fenton in pet bottles of wild enteric bacteria of natural well water: Absence of re-growth after one week of subsequent storage. Appl Catal B Environ 129:309–317 . doi: 10.1016/j.apcatb.2012.09.016

80. Quansah DA, Adaramola MS, Mensah LD (2016) Solar Photovoltaics in Sub-Saharan Africa – Addressing Barriers, Unlocking Potential. Energy Procedia 106:97–110 . doi: https://doi.org/10.1016/j.egypro.2016.12.108

New insight into the microstructure of natural calcined laterites and their performance as heterogeneous Fenton catalyst for methylene blue degradation

Gloria Murielle Rostandi KPINSOTON[1,2], Héla KAROUI[1], Yohan RICHARDSON[2*], Blédja N'dri Stéphanie KOFFI[1], Hamma YACOUBA[3], Julius MOTUZAS[4], Martin DROBEK[5], Abdou LAWANE GANA[6]

1. Institut International d'Ingénierie de l'Eau et de l'Environnement (2iE), Laboratoire Eau Dépollution Ecosystème et Santé (LEDES), Rue de la Science, 01 BP 594 Ouagadougou 01, Burkina Faso.
2. Institut International d'Ingénierie de l'Eau et de l'Environnement (2iE), Laboratoire Biomasse Energie et Biocarburants (LBEB), Rue de la Science, 01 BP 594 Ouagadougou 01, Burkina Faso.
3. Institut International d'Ingénierie de l'Eau et de l'Environnement (2iE), Laboratoire Hydrologie et Ressources en eau (LEAH), Rue de la Science, 01 BP 594 Ouagadougou 01, Burkina Faso.
4. The University of Queensland, FIM2Lab – Functional Interfacial Materials and Membranes, School of Chemical Engineering, Brisbane, Qld 4072, Australia.
5. Institut Européen des Membranes, UMR 5635, Université de Montpellier, ENSCM, CNRS, Place Eugène Bataillon, F-34095 Montpellier cedex 5, France.
6. Institut International d'Ingénierie de l'Eau et de l'Environnement (2iE), Laboratoire Eco-matériaux de construction (LEMC), Rue de la Science, 01 BP 594 Ouagadougou 01, Burkina Faso.

*corresponding author: Yohan RICHARDSON. Email : richardson.yohan@gmail.com

Supplementary information

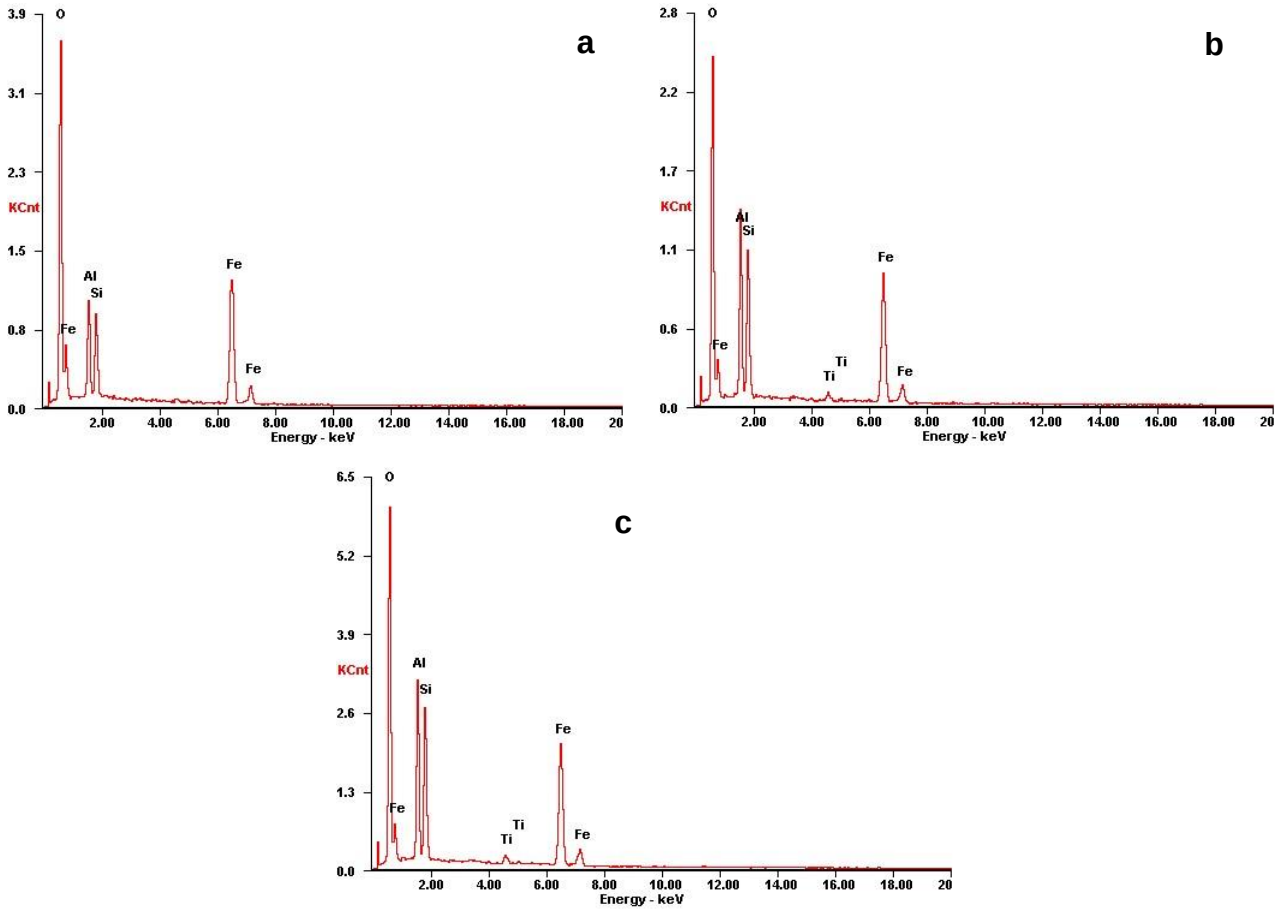

Fig. S1 EDS spectra of the raw laterite sample (RL) recorded on three different areas of a SEM image. a. Area 1; b. Area 2, c. Area 3.

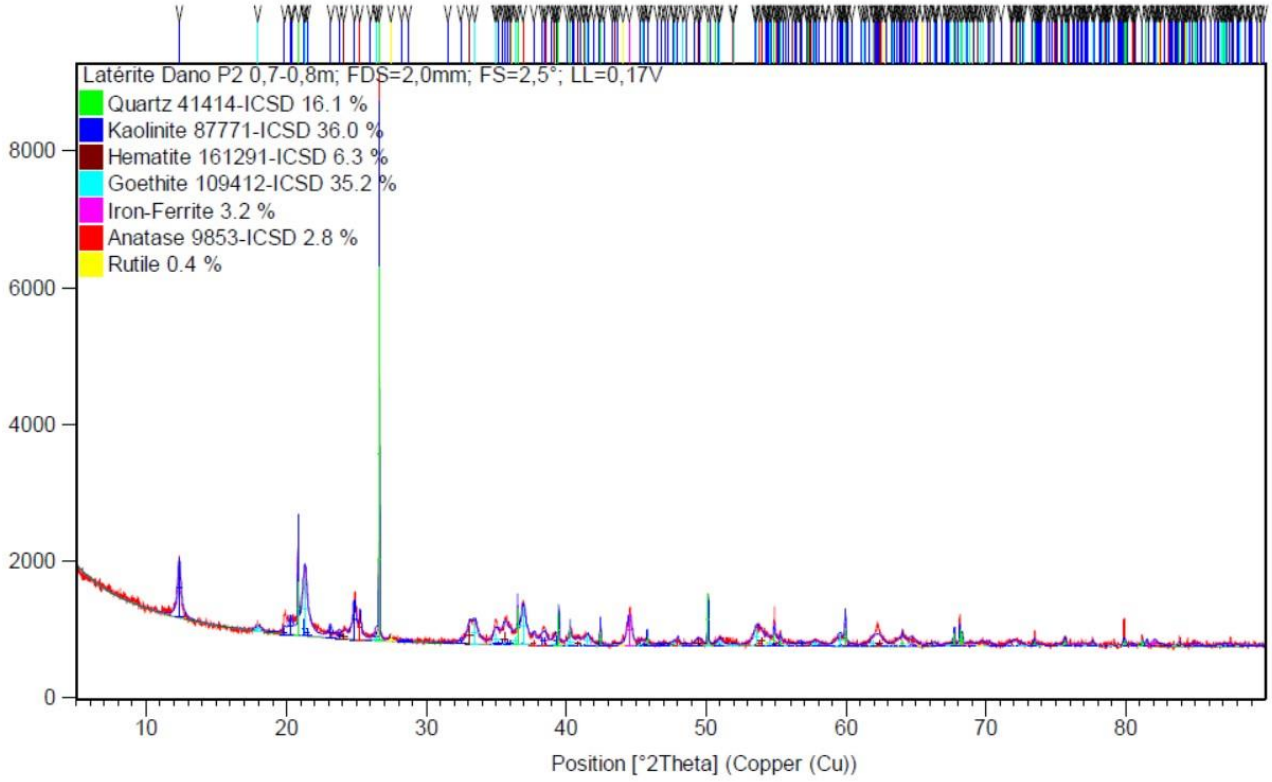

Fig. S2 XRD pattern of the raw laterite sample (RL) with the result of the Rietveld refinement

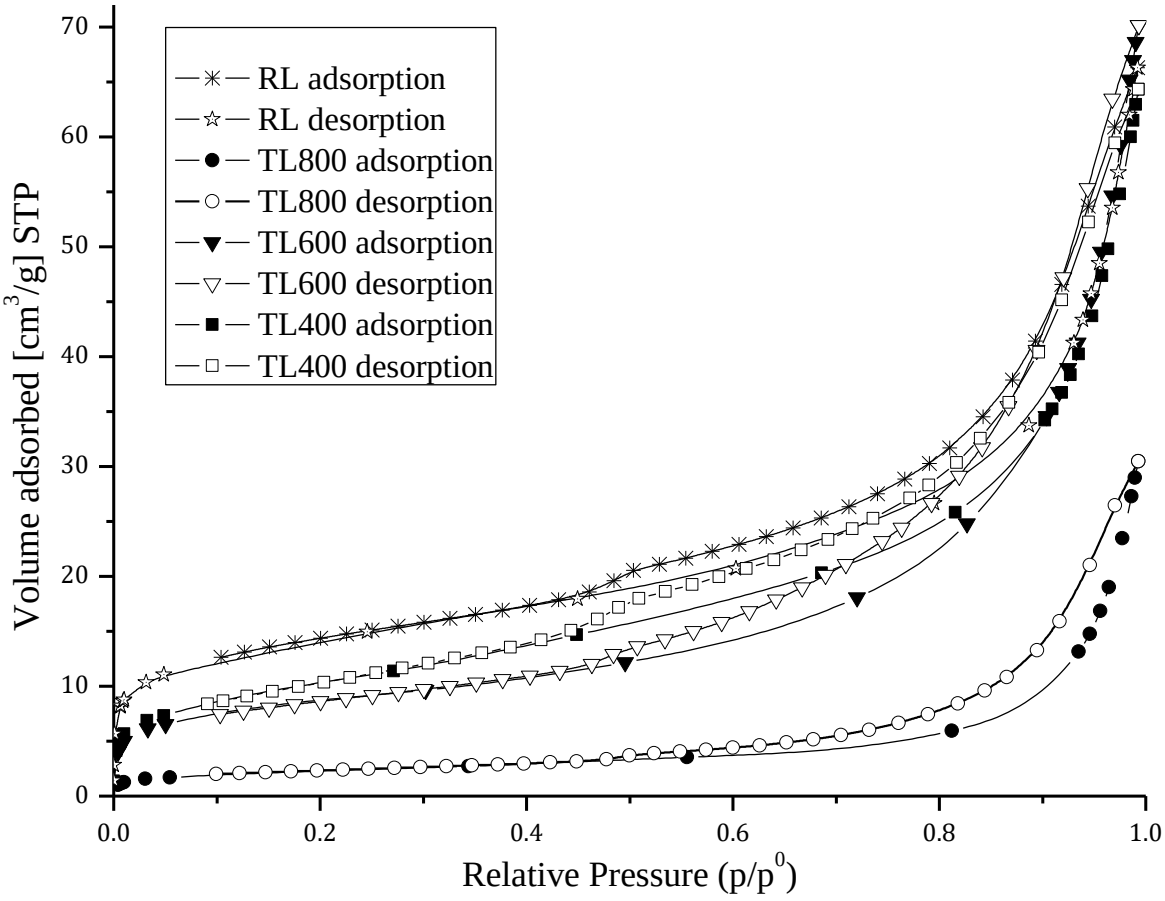

Fig. S3 N_2 adsorption desorption isotherms of raw laterite and calcined laterites.

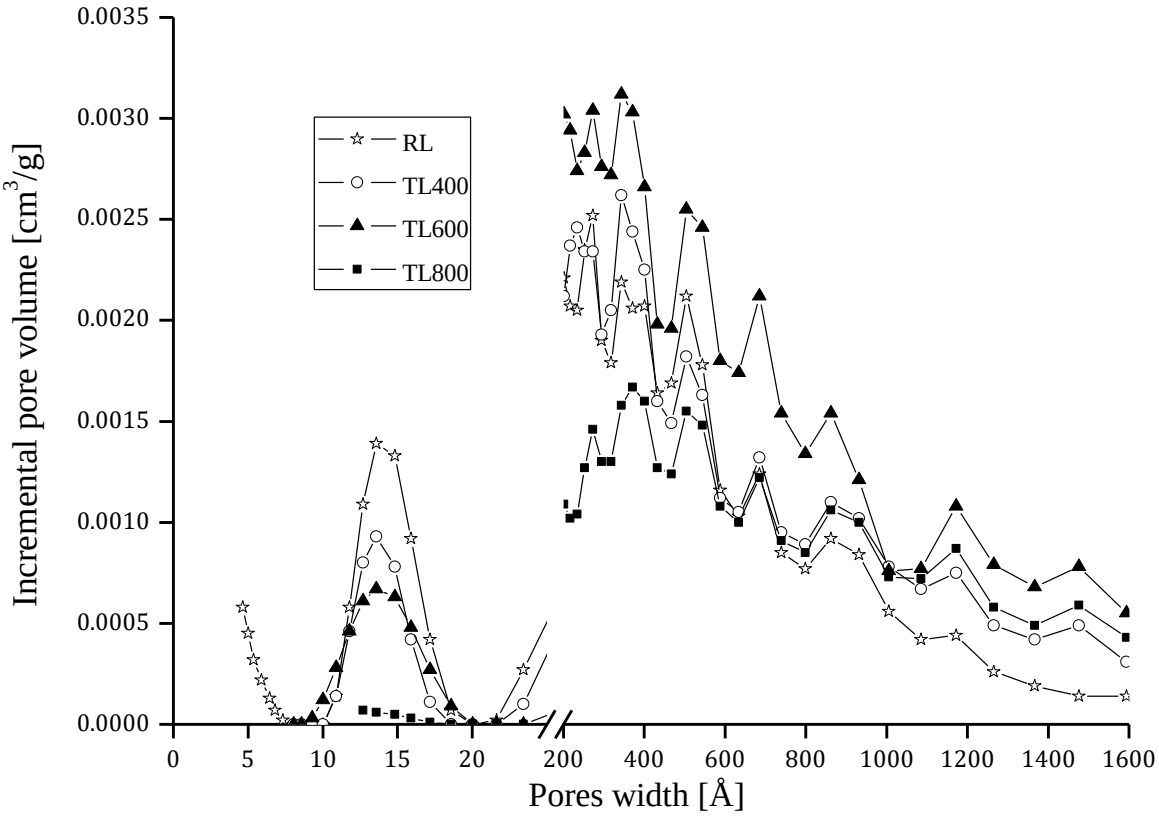

Fig. S4 Pore size distribution from DFT model for raw laterite and calcined laterites.